M. Henke, G. Gerlach

A multi-layered variable stiffness device based on smart form closure actuators

Erstveröffentlichung in / First published in:

Journal of Intelligent Material Systems and Structures. 2016, 27(3), S. 375 - 383 *[Zugriff am: 12.08.2019]*. SAGE journals. ISSN 1530-8138.

DOI: https://doi.org/10.1177/1045389X15577645

Journal of
Intelligent Material
Systems and Structures

Original Article

Journal of Intelligent Material Systems and Structures
2016, Vol. 27(3) 375–383

DOI: 10.1177/1045389X15577645
jim.sagepub.com
SAGE

A multi-layered variable stiffness device based on smart form closure actuators

M Henke and G Gerlach

Abstract

This contribution describes the properties and limitations of multi-layered mechanical devices with variable flexural stiffness. Such structures are supposed to be components of new smart, self-sensing and self-controlling composite materials for lightweight constructions. To enable a proper stiffness control, reliable actuators with high actuation capabilities based on smart materials are used. Those actuators are either driven by electroactive polymers (EAPs) or shape memory alloy (SMA) wires. They control the area moment of inertia of the multi-layered bending structures. To change the area moment of inertia and, hence, the flexural stiffness of an multi-layered beam within a wide range, it is necessary to stack as many layers as possible over each other. The fundamental function of this approach is demonstrated with a three-layer stack consisting of three independent layers and four form closure actuators driven by SMAs. This experimental set-up was able to change its bending stiffness k by a factor of 14.6, with a minimum and maximum stiffness of $k_{min} = 0.11\ N\ mm^{-1}$ and $k_{max} = 1.73\ N\ mm^{-1}$, respectively. The usage of four independently controllable actuators yields nine independent flexural-stiffness states of the beam. Both analytical and numerical calculations have shown good agreement with the measured stiffness values.

Keywords

variable stiffness, multi-layer, shape memory alloy, electroactive polymer

Introduction

For several decades, there have been great efforts to develop smart, self-sensing and self-controlling materials which can adapt their material properties upon changing environmental conditions (e.g. Crawley, 1994; Kornbluh et al., 2004; Rogers et al., 1988; Srinivasan and McFarland, 2001). Another method, which is considered here, is to use structures with variable stiffness, which are able to change their bending stiffness by several orders of magnitude. In the last few years a variety of studies has been dedicated to this topic, especially with respect to lightweight structures and aviation technologies.

The stiffness control can be achieved in different ways. One possibility is to influence the internal structure of a structural component. Florance et al. (2004) discussed approaches to directly changing the flexural stiffness of airfoils by changing the orientation of internal struts, which influences the area moment of inertia and, thus, the flexural stiffness of the airfoil. A similar way to change the stiffness of robotic arms was described by Hollander and Sugar (2004) and Sugar and Hollander (2009), who changed the stiffness by turning a beam with rectangular cross-section.

Runge et al. (1988) demonstrated flexural stiffness control by changing the sheer transmission behavior of struts within airfoils. The struts comprised two independent components which could connect the loose strut parts. If the strut parts were not connected then the airfoil was compliant because the struts were not able to transfer sheer stresses and could slide against each other. If the strut parts were connected then they became rigid and the airfoil was stiffened.

Kawamura et al. (2002) described a similar approach. They stacked several independent thin metal layers over each other and positioned them within a balloon-like structure. By applying a vacuum to the balloon, the layers were pressed together by the

Solid-State Electronics Laboratory, TU Dresden, Germany

Corresponding author:
M Henke, Solid-State Electronics Laboratory, TU Dresden, Helmoltzstr. 18, Dresden 01069, Germany.
Email: markus.henke@tu-dresden.de

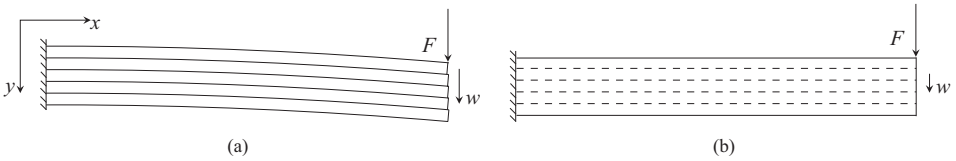

Figure 1. Multi-layered beam in its (a) compliant and (b) stiff state.

external air pressure. This generated friction between the layers, thus enabling the transmission of sheer stresses and stiffening the multi-layered beam structure. Without vacuum the beam becomes compliant.

Multi-layered beams with controllable area moment of inertia can change their flexural stiffness by more than one order of magnitude by controlling the inter-layer slip using adjustable friction forces (Henke and Gerlach, 2013, 2014b). However, the maximum generated friction forces limit the maximum load applicable to the multi-layer beam and, hence, its fields of application. Instead of friction forces also form closure can be used to transfer larger sheer stresses. This enables the beams to take more load (Henke et al., 2012c).

To switch between several independent stiffness states by form closure, it is necessary to locate switching actuators within the multi-layer beam, which reliably control the sliding between adjacent layers. In practical applications it is often advantageous to vary the flexural stiffness of structures in a wide range. Therefore, it is necessary to stack a certain amount of independent layers over each other within the beam. This requires that form closure actuators have to be very flat but also have to generate large actuation. This contradiction can be solved by using smart materials such as electroactive polymers (EAPs) and shape memory alloys (SMAs) (Henke et al., 2012a,b, 2013).

The following contribution is focused on fundamental investigations to build up multi-layer devices based on smart material actuators with tunable flexural stiffnesses. Only the steady-state behavior will be discussed in this paper. The basic functionality widely differs from the principles shown in Vos and Barret (2010).

Stiffness control by varying the area moment of inertia

The flexural stiffness k of a multi-layered bending beam is defined as the ratio between an external load F and a resulting deflection w at the force application point:

$$k = \frac{F}{w} \tag{1}$$

Considering a multi-layered stack consisting of N independent layers (Figure 1) its bending stiffness depends both on material and geometrical parameters, such as the Young's modulus Y and the length l, width b and thickness h of the beam. When all layers are allowed to freely slide over each other (Figure 1(a)), the total bending stiffness equals the sum of the bending stiffnesses of all individual beams:

$$k = N\frac{YI}{l^3} \tag{2}$$

Considering the area moment of inertia of a beam with rectangular cross-section, the Pilkey (1994) equation (2) yields

$$k_{\min} = NYb\left(\frac{h}{l}\right)^3 \tag{3}$$

Contemplating the same beam, when the inter-layer sliding is suppressed (Figure 1(b)), the structure acts as a homogeneous rigid beam. Hence, the height of the whole structure equals $H = Nh$ and equation (3) yields

$$k_{\max} = Yb\left(\frac{Nh}{l}\right)^3 \tag{4}$$

Therefore, the ratio $K_{\max}$ between the maximum and the minimum stiffness values $k_{\min}$ and $k_{\max}$, respectively, equals

$$K_{\max} = \frac{k_{\max}}{k_{\min}} = N^2 \tag{5}$$

In other words, the flexural stiffness of a multi-layered beam with N independent layers can be varied by the ratio of N^2 by adjusting its inter-layer slip. By only changing the inter-layer slip locally, it is also possible to build up structures with even more stiffness states up to nearly continuously tunable stiffness devices (Henke and Gerlach, 2013, 2014b).

Stiffness control via form closure

Basic function

To reliably adjust the sliding behavior between the independent layers it is necessary to switch between states with and without form closure. For that reason, so-called form-closure actuators are used, which possess form-closure structures consisting of teeth and gaps, corresponding to those of the independent beam layers. Thus, the actuators are able to lock to avoid the sliding between the beam layers by driving their form-closure

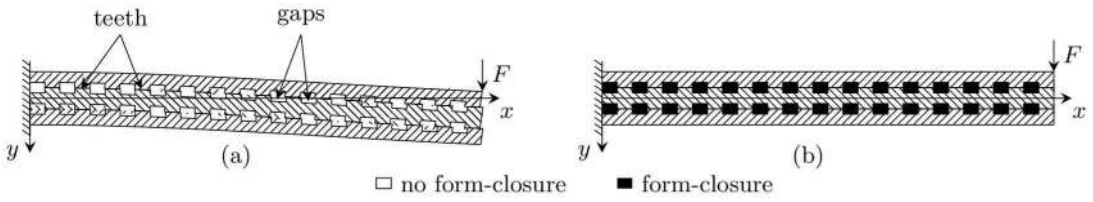

Figure 2. Schematic side view of a three-layered bending beam with controllable stiffness bases of form closure.

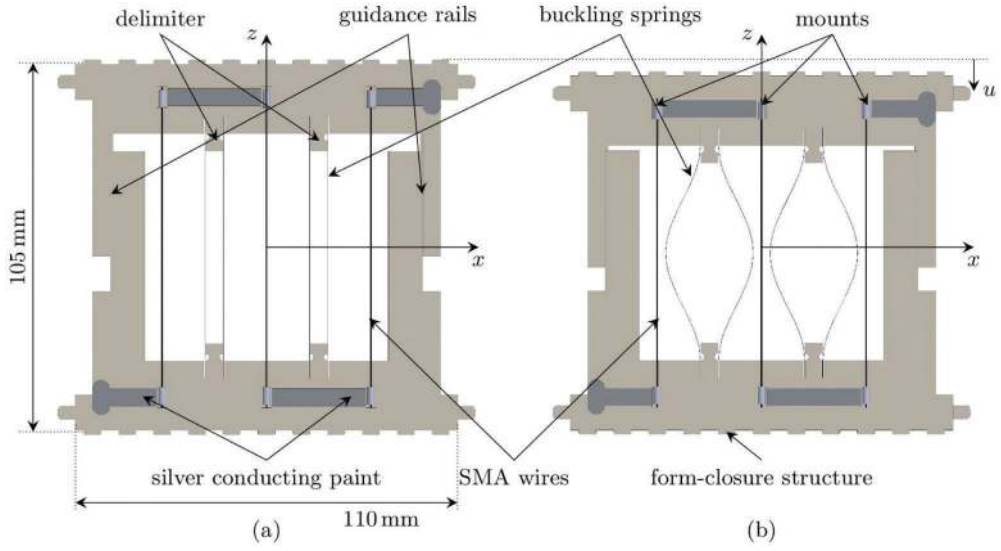

Figure 3. SMA-driven form-closure actuator in (a) initial and (b) activated state.

structure in those of adjacent beam layers. The actuators are driven by SMA wires and are able to change their overall length by nearly 5%. Figure 2 shows the schematic function of such a form-closure set-up. In Figure 2(a) the actuators, which are located between two corresponding layers, are activated and shortened. In this state the actuators do not prevent the interlayer sliding and the beam is in its compliant state.

If the actuators are not activated and elongated, their teeth and gaps fix the inter-layer sliding by form closure, as depicted in Figure 2(b).

Form-closure actuators

The form closure actuators (Figure 3) are built up of two independent parts, which are produced by selective laser sintering. Both parts can slide against each other and are connected by an integrated guidance rail. The actuators possess an overall thickness $t_{act} = 2.8$ mm, which is slightly smaller than the height $h_{gap} = 3$ mm of the actuator gaps between two adjacent layers. The remaining gap enables an actuation.

To control the form closure between the independent layers, it is required that the used actuators generate a high enough actuation force and deflection to ensure form closure. Simultaneously, it is necessary that the actuators are very flat to fit between adjacent beam layers. For that reason, shape memory wires were chosen to drive the actuators. Due to commercial availability, SmartFlex wires with a diameter $d = 200\mu$m (SAES Getters, Italy) were used. If they are resistively heated above the activation temperature $T_{act} \approx 95°$C they shorten by about 5%. Thereby, they produce a blocking force $F_{block}^{SMA} \approx 19$N corresponding to a working force $F_{work} = 5$N per wire.

When the temperature falls below T_{act}, the wires elongate until they reach their initial length. Four buckling springs with a total blocking force $F_{block}^{Spr} = 12.8$N support this elongation and keep the actuator in its initial length, where no heating current is applied. Integrated delimiters ensure, that the springs buckle in the right direction. Since the wires are able to generate a higher working force $F_{work}^{tot} < F_{block}^{Spr}$, the actuators are able to shorten upon the application of an electrical current through the wires. Therefore, the three wires are electrically connected in series via silver conductive paint and are mechanically connected in parallel. Crimping shucks are used to fixate them in the

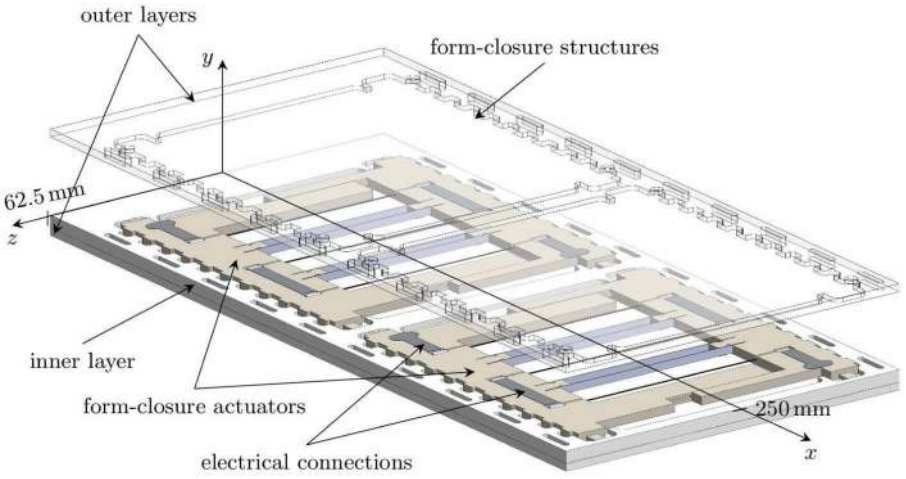

Figure 4. Demonstrator with three-layer set-up, comprising of three individual layers and four planar actuators driven by SMA wires.

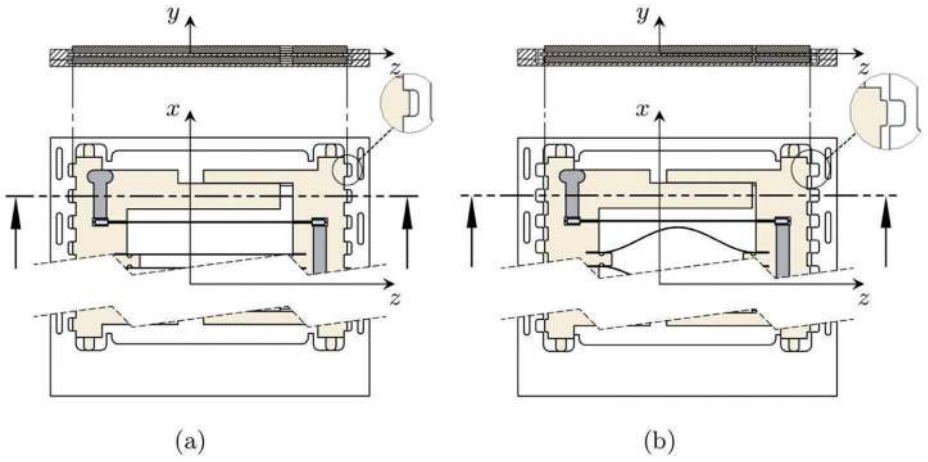

Figure 5. Switching mechanism of the set-up of Figure 4, without depicting the uppermost layer. If the actuators are not activated and in its initial state (a), then form closure is activated and the layers cannot slide over each other. If the actuators are activated and shortened (b), then there is no form closure and the layers can slide over each other.

actuator. Figure 3 shows a single actuator in its initial and its activated state, respectively. A detailed description of those actuators, its characteristics and mathematical models are presented in Henke and Gerlach (2014a).

Demonstrator set-up

The demonstrators studied here (Figure 4) consist of three independent layers (three-layer beam) and four actuators. However, all theoretical considerations can easily be adapted to multi-layer beams with more layers.

The middle layer carries two form-closure actuators having two form-closure structures each possessing two rows of teeth. The latter match to rows of teeth in both the top and the bottom layer. Depending on the actuation state of the actuators the teeth of the form-closure structures of the actuators latch in the rows of teeth in the top and the bottom layers, hence creating a stiff connection between all three layers. Because the actuator height amounts to twice the height of the form-closure structures of the layers, the actuators can hinder the sliding between the layers. Figure 5 depicts the switching mechanism in detail. In Figure 5(a) the actuators are in their initial, elongated state. As can be seen, the form-closure structures of the actuators fit in those of the layers and hinder a movement of the layers against each other via form closure. Thus, the beam structure is in its stiff state. In Figure 5(b) the actuators are activated and shortened. Therefore, remains a gap between the form-closure structures of the actuators and layers. Thus, the layers are able to slide against

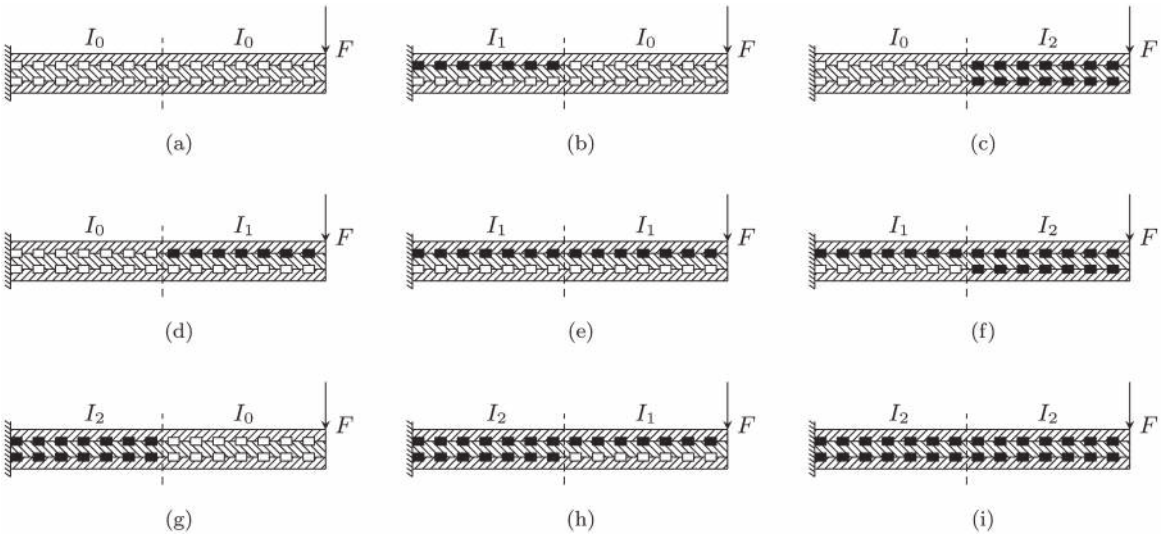

Figure 6. Three-layer beam with four form-closure actuators with nine different stiffness states. Black areas depict teeth of the form-closure actuators latched onto the teeth of the middle and the rows of teeth of the corresponding outer layers.

each other. The beam structure is in a more compliant state.

The layers are manufactured by rapid-prototyping (stereo-lithography, Somos NeXt resin by DSM Somos). The overall thickness of the outer layers is $t_{out} = 3$ mm, where both the layer skin and the form-closure structures have a thickness of $t_{fc} = 1.5$ mm. Since the middle layer comprises two form-closure structures at the bottom and the top the overall thickness amounts to $t_{mid} = 4.5$ mm. This yields an total thickness of the whole set-up of $t_{tot} = 7.5$ mm.

Because all four actuators in the three-layer set-up can be excited independently, it is possible to switch between nine different stiffness states (Figure 6). In Figure 6(a) no actuator avoids the sliding between the layers. Therefore, the layers can freely slide over each other and the beam is in its most compliant state ($k_1 = k_{min}$). In this state the whole structure has its minimum area moment of inertia I_0. When only the upper two actuators hinder the sliding of the upper two layers (Figure 6(g)), the demonstrator is in an intermediate stiffness state and shows an area moment of inertia I_1. Figure 6(i) depicts the set-up, when all actuators are latched and hinder the inter-layer sliding and the beam is in its stiffest state, where $k_9 = k_{max}$ and $I = I_2$. Therefore, the three-layer structure of Figure 4 shows three different area moments of inertia in two sections. The number of possible stiffness states depends both on the number of independent area moments of inertia and on the number of independent sections. If N_I is the number of possible area moments of inertia and N_{sec} is the number of independent sections, the number of possible stiffness states N_{stiff} yields

$$N_{stiff} = N_I^{N_{sec}} \tag{6}$$

$$N_{stiff} = 3^2 = 9 \tag{7}$$

Mathematical models

In order to estimate the bending stiffness k of the whole structure, a simple analytic model is used. It allows the estimation of the geometrical parameters of the demonstrator and of the ratio K_{max} between the maximum and minimum stiffnesses:

$$K_{max} = \frac{k_{max}}{k_{min}} \tag{8}$$

To consider the complicated geometry of the demonstrator set-up in detail a finite-element (FE) model was used. These calculations were performed using the FE-tool ABAQUS.

Analytic model

To estimate the ratio K_{max} Castigliano's method is used (Pilkey, 1994). It states that the deflection w of a beam at the force application point can be calculated as deviation of the strain energy U with respect to the applied force F:

$$w = \frac{\partial U}{\partial F} \tag{9}$$

The compliance n is now given as deviation of the deflection w with respect to the applied force F at the force application point and as the inverse of the stiffness k:

$$n = \frac{1}{k} = \frac{\partial w}{\partial F} = \frac{\partial^2 U}{\partial F^2} \tag{10}$$

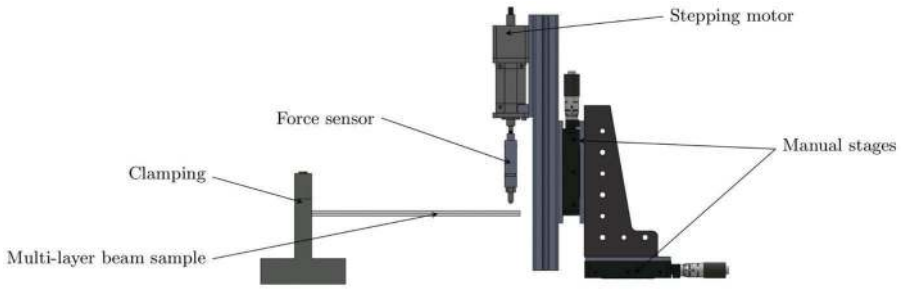

Figure 7. Measurement set-up to measure deflection *w* and resulting force *F* simultaneously.

Due to simplicity reasons pure bending is assumed and sheer stresses and normal forces are neglected. Then the strain energy of the beam is given as (Henke and Gerlach, 2014b; Pilkey, 1994)

$$U_i(x) = \int_{x_0}^{x} \frac{1}{2} \frac{M_{\mathrm{Bz}}^2(x')}{YI_i} \, \mathrm{d}x' \tag{11}$$

with the bending moment $M_{\mathrm{Bz}}(x)$, Young's modulus Y and the area moment of inertia I. Considering the demonstrator in Figures 4 and 6 the strain energy has to be calculated for three independent areas, because the area moment of inertia can be switched independently in the different actuator sections. A small section between the actuator cannot be stiffened and has always a constant area moment of inertia I_{p}. Therefore, equation (11) yields

$$\begin{aligned} n = \frac{1}{k} = \frac{\partial}{\partial F} \Bigg[& \int_0^{l_{\mathrm{I}}} \frac{M_{\mathrm{Bz}}(x)}{YI_1} \frac{\partial M_{\mathrm{Bz}}(x)}{\partial F} \, \mathrm{d}x \\ & + \int_{l_{\mathrm{I}}}^{l_{\mathrm{I}} + l_{\mathrm{p}}} \frac{M_{\mathrm{Bz}}(x)}{YI_2} \frac{\partial M_{\mathrm{Bz}}(x)}{\partial F} \, \mathrm{d}x. \\ & + \int_{l_{\mathrm{I}} + l_{\mathrm{p}}}^{l_{\mathrm{I}} + l_{\mathrm{p}} + l_{\mathrm{II}}} \frac{M_{\mathrm{Bz}}(x)}{YI_3} \frac{\partial M_{\mathrm{Bz}}(x)}{\partial F} \, \mathrm{d}x \Bigg] \end{aligned} \tag{12}$$

with the area moments of inertia I_{I}, I_{II}, I_{p} in the first, the second and the passive area, respectively.

However, this model is only valid for the stiffness states (a) and (c), and only by approximation for the states (b), (e), (g) and (i). Therefore, it is only possible to calculate the maximum theoretical stiffness ratio between k_{i} and k_{a} according to equation (11) during the design process of the demonstrator set-up. A comparison between the corresponding analytical and experimental results is given in section on "Results". Cases where the suppressed inter-layer sliding in the right section of the flexural beam also influences the behavior in the left section cannot be taken into account with this model because equation (12) does only depends on the area moments of inertia in the different sections, but not on their mutual interface.

Equation (12) can be used to calculate the maximum stiffness ratio between the stiffest and the most compliant states and to examine the influence of the length of the passive section. The area moments of inertia for every state and section were calculated based on the parallel axis theorem, taking into account both the layers and the actuators (Henke, 2014).

FE model

To study the mechanical behavior of 3D flexural beams in more detail, a FE model was used based on the FE program package ABAQUS. As for the analytical analysis one end of the beam structure was fixed and a force was applied at the free end. The stiffness was calculated from the resulting force–deflection relationship. The comparison of the analytical and the FE analysis with experimental results are show in the following section. A maximum stiffness change $K_{\max}$ of the order of 20–30 can be expected.

Experimental investigations

Figure 7 schematically depicts the measurement set-up. The clamping and the bottom manual stage were mounted to a breadboard (MB6060/M, Thorlabs). The demonstrator set-up from Figure 4 was used for experimental investigations. One end of the flexural beam was clamped and the other, free end was deflected by a stepping motor (L4118, Nanotec, Germany) cyclically. This stepping motor includes an optical encoder (WEDL5546-A10, Nanotec, Germany), which is used to measure the position of the stepping motor and, hence, the deflection w of the sample. The resulting force was measured by a load cell (KAP-S/10N/0,1, A.S.T. GmbH, Germany), which was analyzed by a hand-held device (AE 703, A.S.T. GmbH, Germany). To control the electrical current through the SMA wires a remote power supply (PS 2342-10B, Elektro-Automatik, Germany). To drive the stepping motor and the power supply and simultaneously measure the force and deflection, all active parts of the presented measurement set-up were connected to a PC (Dell XPS) and controlled via the LabView program.

To reduce measurement uncertainties, measurement cycles were run a minimum of 10 times and the

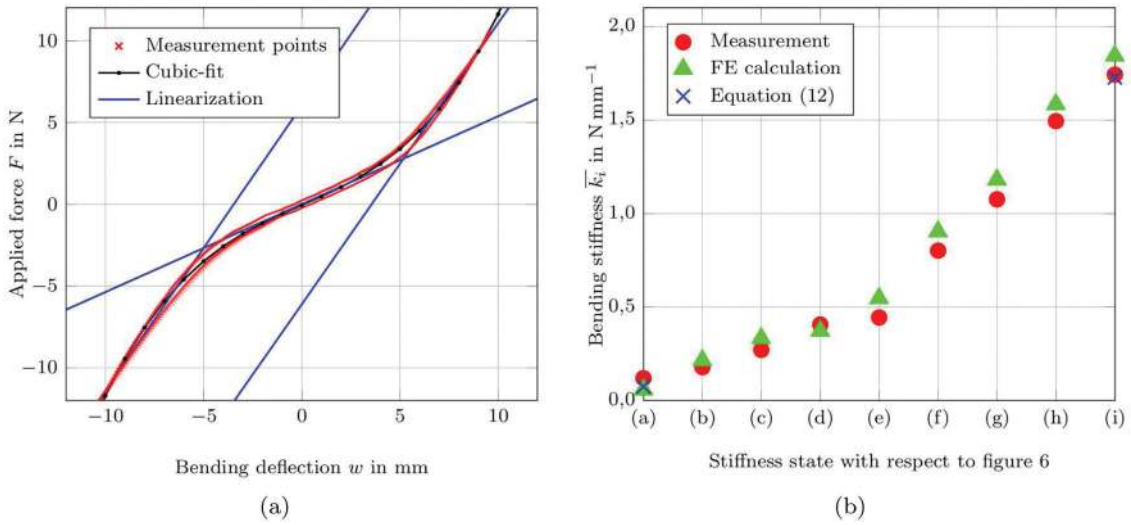

Figure 8. Measurement results: (a) force–deflection characteristic for the described demonstrator set-up with cubic fit and linearizations for stiffness state (i) from Figure 6; (b) comparison between the analytical and numerical calculations and the measured stiffnesses.

systematic measurement deviation caused by the compliance of the load cell ($n_{\text{meas}} = 0.04$ mmN^{-1}) was eliminated individually for every measurement point by the LabView software. The maximum deflection in both directions was $w_{\max} = 10$ mm. To measure the quasi-static stiffness change, the sample was deflected with maximum speed of $v_{\text{def}} = 0.5$ mm. The average resolution of measurement points depends on the speed of the LabView software and amounts to $\Delta w = 0.1$ mm. This procedure was performed for all the stiffness states shown in Figure 6.

Results

The aim of the measurements is to determine the flexural stiffnesses of the demonstrator set-up for every stiffness state and to refer them to the initial stiffness k_a (Figure 6(a)). Owing to high nonlinearity during the measurement cycles it is necessary to evaluate the measurement points separately for every stiffness state.

Determination of the static stiffnesses k_i

The analysis of the measurement points has shown high nonlinearity of the force–deflection curves and, hence, the stiffnesses. Figure 8(a) shows the characteristic stiffness curve, that is force–deflection curve, of the demonstrator in its stiffest state (Figure 6(i)). For large positive and large negative deflections the curves are similar, even if the curves show a shift to the right (for positive deflections) and to the left (for negative deflections) and show nearly the same stiffness values. The bottom stiffness k_b for negative deflection yields 1.740 N mm^{-1}, whereas the upper stiffness for positive deflections yields $k_u = 1.720$ N mm^{-1}. The intermediate part of the curve for small deflections $|w| < 4$ mm in the origin (at $F = 0$, $w = 0$) possess a much slower slope. The difference between these curves is caused by a small mechanical clearance between the form-closure structures at the actuators and the layers. The intermediate part describes the transition where the layers can slide over each other until this clearance is overcome.

The curve in Figure 8(a) shows two characteristic points as intersections of the intermediate straight line with lower slope and the both straight lines with larger slope. These points determine the states where the form closure comes in full operation for larger deflections. The true stiffness of every stiffness state is only reached for deflections higher than $|w| > 6$ mm.

To determine the stiffness for large deflections the measurement data was fitted to a cubic function

$$F(w) = aw^3 + bw^2 + cw + d \tag{13}$$

The stiffness values k_u and k_l were calculated for the curve parts with higher slope where $k_{u\,i}$ and $k_{l\,i}$ mean the stiffness values of the upper and the lower part, respectively, and i describes the stiffness state with respect to Figure 6(a)–(i). The average stiffness then yields

$$\overline{k_i} = \frac{|k_{l_i} - k_{u_i}|}{2} \tag{14}$$

In addition to the described nonlinearity, there are also creep effects after switching between different stiffness states. This is caused by the used polymer materials, related to rapid prototyping processes. The force–

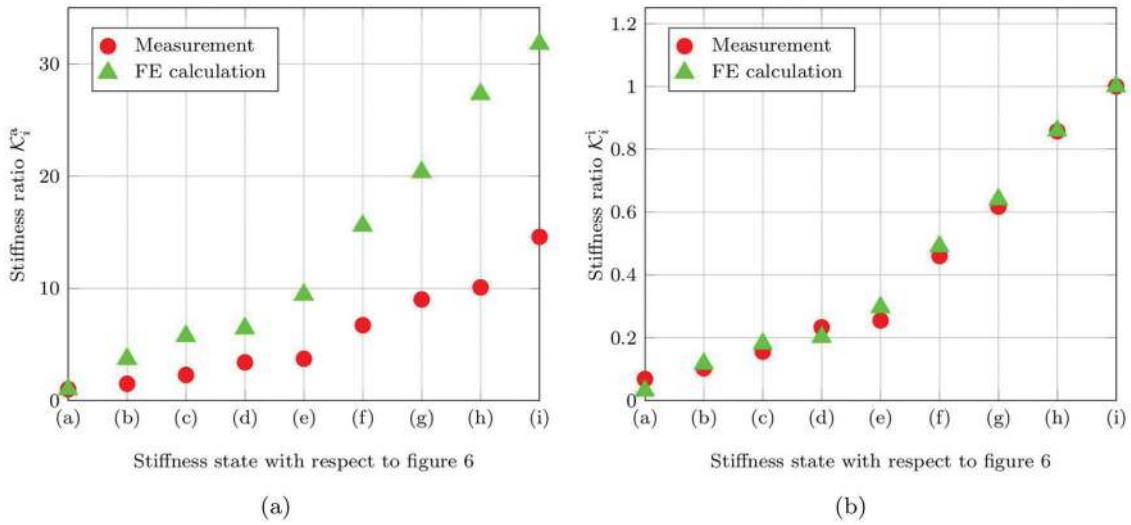

Figure 9. Comparison between the analytical and numerical calculation results and the measurement results for the stiffness ratio (a) $K_i^a = \frac{k_{ki}}{k_a}$ and (b) $K_i^i = \frac{k_{ki}}{k_i}$ according to the stiffness sates from Figure 6.

deflection curves approach the final shape within the first few deflection cycles. Furthermore, there are also hysteresis effects, probably caused by remaining slip and, hence, friction between the layers. This applies also to stiff states, where the sliding is locked by the form-closure actuators. The hysteresis falls with rising stiffness.

Figure 8(b) compares the measured and the calculated results for the static flexural stiffnesses k_i for every stiffness state i from Figure 6, both for analytical and numerical calculations. It can be seen that the calculated values agree very well with the measured data. The stiffness $\bar{k}_i$ for the stiffness state (a) shows a relatively large difference between the measured and calculated values. Here, the measured value amounts to twice the value which was calculated analytically and numerically. The difference is caused by large friction between the layers because the sliding regards the largest possible area between the layers.

Determination of the stiffness ratios K^a and K^i

To determine the stiffness ratios K^a and K^i, the evaluated stiffness $\bar{k}_i$ values according to equation (14) are used

$$K_i^a = \frac{\bar{k}_i}{\bar{k}_a}, \quad K_i^i = \frac{\bar{k}_i}{\bar{k}_i} \tag{15}$$

Here, the values K_i^a describe the ratio between the particular stiffnesses in the stiffness states and the lowest stiffness k_a, and the values K_i^i describe those between the particular stiffnesses and the highest stiffness k_i. Figure 9 depicts the stiffness ratios K_i^a for all of the different stiffness states. As can be easily seen, the values between the numerical and measurement results differ by about a factor of 2. This is because the numerically predicted stiffness k_a for the most compliant state (a) is only half the measured value. Since the stiffness ratio K_i^a is related to this most compliant state, there occurs a ratio of approximately 2:1 between the calculated and the measured values for the stiffness ratio K_i^a in the remaining stiffness states. The maximum measured stiffness ratio equals $K_i^a = 14.6$, the numerically predicted value yields $K_i^a = 31.8$.

Figure 9(b) depicts the stiffness ratio K_i^i related to the stiffest state k_i. This definition yields a very good agreement between the calculated and the measured stiffness ratios for all stiffness states with the exception of k_a.

Discussion and conclusions

This contribution has described the function principle of a multi-layered beam structure with controllable flexural stiffness based on a layer stack with layers sliding over each other and with form-closure elements which can influence this sliding. The stiffness of such flexural beam structures were calculated analytically and numerically. It turned out that the analytical model only provides acceptable solutions for particular cases.

Experiments were performed using a set-up consisting of three layers and four SMA-driven form-closure actuators. This allowed to switch between nine different stiffness states. The set-up showed a maximum factor of flexural stiffness change of $K_{max}^a = 14.6$. Future investigations should deal with the reduction of friction between the independent layers to enable higher values of K.

To reduce nonlinearity in the force–deflection behavior it would be advantageous to consider the usage of materials with lower creeping effects, such as metals. This would also allow us to fabricate demonstrator set-ups with lower mechanical clearance, which could also lower both creep and hysteresis.

Due to its modular set-up it is easily possible to enlarge the stiffness variation by stacking more layers and to increase the number of individual stiffness states by a larger number of actuators. In such a way structures can easily be adapted to their particular application. Further studies should concentrate on reducing the thickness of the individual layers and actuators in order to achieve higher ratios of stiffness variation with a smaller total height of the layer stack.

Declaration of Conflicting Interests

The author(s) declared no potential conflicts of interest with respect to the research, authorship, and/or publication of this article.

Funding

The author(s) disclosed receipt of the following financial support for the research, authorship, and/or publication of this article: This project was funded by the European Union (ERDF) and the Free State of Saxony (project number 100117154).

References

Crawley EF (1994) Intelligent structures for aerospace – A technology overview and assessment. *AIAA Journal* 32: 1689–1699.

Florance JR, Heeg J, Spain CV, Ivanco TG, Wieseman CD and Lively PS (1994) Variable stiffness spar wind-tunnel model development and testing. In: *45th AIAA/ASME/ASCE/AHS/ASC structures, structural dynamics and materials conference*, Palm Springs, CA, 20–22 April 2004.

Henke M (2014) *Konstruktionselemente mit einstellbarer Biegesteifigkeit*. PhD Thesis, TU Dresden, Germany.

Henke M and Gerlach G (2013) On a high-potential variable flexural stiffness device. In: *Proceedings of SPIE 8763 – Smart sensors, actuators, and MEMS VI*, Grenoble, France, 24–26 April 2013, pp. 876312-1–876312-10.

Henke M and Gerlach G (2014) Mono- and bi-stable planar actuators for stiffness control driven by shape memory alloys. *unpublished*

Henke M and Gerlach G (2014) On a high-potential variable-stiffness device. *Microsystem Technologies* 20: 599–606.

Henke M, Renner A, Fischer WJ and Gerlach G (2012) Novel approaches for self-sensing and -control of smart structures. In: WA Hufenbach (ed.) *Tagungsband Internationales Kolloquium des Spitzentechnologieclusters ECEMP*, 23–24 October 2012, Dresden, Germany, pp. 282–304.

Henke M, Sorber J and Gerlach G (2013) EAP-actuators with improved actuation capabilities for construction elements with controllable stiffness. *Advances in Science and Technology* 79: 75–80.

Henke M, Sorber J and Gerlach G (2012) Actuator for stiffness-control of stacked flexure beams: principle, set-up, design. In: *ACTUATOR* 2012, 18–20 June 2012, Bremen, Germany, pp. 400–403.

Henke M, Sorber J and Gerlach G (2012) Multi-layer beam with variable stiffness based on electroactive polymers. In: Y Bar-Cohen (ed.) *Proceedings of SPIE 8340 – Electroactive polymer actuators and devices (EAPAD) 2012*, San Diego, CA, 11–15 March 2012, pp. 83401P–1–83401P–13.

Hollander K and Sugar T (2004) Concepts for compliant actuation in wearable robotic systems. In: *Proceedings US–Korea conference on science, technology and entrepreneurship (UKC 04)*, Research Triangle Park, NC, 12–14 August 2004, pp. 644–650.

Kawamura S, Yamamoto T, Ishida D, et al. (2002) Development of passive elements with variable mechanical impedance for wearable robots. In: *Proceedings IEEE international conference on robotics and automation, 2002 (ICRA 02)*, 11–15 May 2002, Washington, DC, pp. 248–253.

Kornbluh RD, Prahlad H, Pelrine R, et al. (2004) Rubber to rigid, clamped to undamped: toward composite materials with wide-range controllable stiffness and damping. In: EH Anderson (ed.) *Proceedings of SPIE 5388 – Smart structures and materials 2004: industrial and commercial applications of smart structures technologies*, San Diego, CA, 15–18 March 2004, pp. 372–386.

Pilkey WD (1994) *Formulas for stress, strain, and structural matrices*. New York: Wiley.

Rogers CA, Baker DK and Jaeger CA (1988) Introduction to smart materials and structures. In: CA Rogers (ed.) *Proceedings of U.S. Army Research Office workshop on smart materials, structures and mathematical issues*, Blacksburg, VA, 15–16 September 1988, pp. 17–28.

Runge JB, Osmont D and Ohayon R (2013) Twist control of aerodynamic profiles by a reactive method (experimental results). *Journal of Intelligent Material Systems and Structures* 24: 908–923.

Srinivasan AV and McFarland DM (2001) *Smart structures: analysis and design*. Cambridge: Cambridge University Press.

Sugar T and Hollander K (2009) US7527253B2 *Adjustable stiffness leaf spring actuators*, 5 May 2009.

Vos R and Barret R (2010) Dynamic elastic-axis shifting: an important enhancement of piezoelectric postbuckled precompressed actuators. *AIAA Journal* 48: 583–590.